LAWRENCE
LIVERMORE
NATIONAL
LABORATORY

Charge Exchange Spectra of Hydrogenic and He-like Iron

B. J. Wargelin, P. Beiersdorfer, P. A. Neill, R. E. Olson, J. H. Scofield

May 3, 2005

Disclaimer

This document was prepared as an account of work sponsored by an agency of the United States Government. Neither the United States Government nor the University of California nor any of their employees, makes any warranty, express or implied, or assumes any legal liability or responsibility for the accuracy, completeness, or usefulness of any information, apparatus, product, or process disclosed, or represents that its use would not infringe privately owned rights. Reference herein to any specific commercial product, process, or service by trade name, trademark, manufacturer, or otherwise, does not necessarily constitute or imply its endorsement, recommendation, or favoring by the United States Government or the University of California. The views and opinions of authors expressed herein do not necessarily state or reflect those of the United States Government or the University of California, and shall not be used for advertising or product endorsement purposes.

Charge Exchange Spectra of Hydrogenic and He-like Iron

B. J. Wargelin[1], P. Beiersdorfer[2], P. A. Neill[3], R. E. Olson[4], and J. H. Scofield[2]

ABSTRACT

We present H-like Fe XXVI and He-like Fe XXV charge-exchange spectra resulting from collisions of highly charged iron with N_2 gas at an energy of ~ 10 eV amu^{-1} in an electron beam ion trap. Although high-n emission lines are not resolved in our measurements, we observe that the most likely level for $Fe^{25+} \rightarrow Fe^{24+}$ electron capture is $n_{max} \sim 9$, in line with expectations, while the most likely value for $Fe^{26+} \rightarrow Fe^{25+}$ charge exchange is significantly higher. In the Fe XXV spectrum, the Kα emission feature dominates, whether produced via charge exchange or collisional excitation. The Kα energy centroid is lower in the former case than the latter (6666 versus 6685 eV, respectively), as expected because of the strong enhancement of emission from the forbidden and intercombination lines, relative to the resonance line, in charge-exchange spectra. In contrast, the Fe XXVI high-n Lyman lines have a summed intensity greater than that of Lyα, and are substantially stronger than predicted from theoretical calculations of charge exchange with atomic H. A discussion is presented of the relevance of our results to studies of diffuse Fe emission in the Galactic Center and Galactic Ridge, particularly with *ASTRO-E2*.

Subject headings: atomic data — atomic processes — X-rays: diffuse background — X-rays: general

[1]Smithsonian Astrophysical Observatory, Harvard-Smithsonian Center for Astrophysics, 60 Garden Street, MS-70, Cambridge, MA 02138; bwargelin@cfa.harvard.edu

[2]Department of Physics, Lawrence Livermore National Laboratory, Livermore, CA 94550

[3]Department of Physics, University of Nevada, Reno, NV 89557

[4]Department of Physics, University of Missouri, Rolla, MO 65401

1. INTRODUCTION

Within the past decade, astrophysical X-ray emission via charge exchange (CX) has been recognized to occcur in comets, the atmospheres of planets including the Earth, throughout the heliosphere, and around other stars (see review by Cravens (2002) and references therein). Recently, observations with moderate spectral resolution by *Chandra* (Wargelin et al. 2004; Smith et al. 2005) and *XMM-Newton* (Snowden, Collier, & Kuntz 2004) have detected clear signatures of geocoronal and heliospheric CX, most prominently in time-variable oxygen line emission, which may contribute a significant fraction of the soft X-ray background. All the aforementioned CX emission is from moderately ionized species such as He-like and H-like C, N, O, and Ne which originate in solar or stellar coronae. Those ions emit X rays when they CX with: neutral molecules such as H_2O in comets; neutral H in the Earth's outer atmosphere; and neutral interstellar H and He within the heliosphere or astrospheres around other stars.

CX has also been proposed (Tanaka, Miyaji, & Hasinger 1999) to explain some and perhaps most of the line emission from more highly ionized species such as He-like and H-like Si, S, Ar, Ca, and Fe seen in diffuse emission from the Galactic Ridge (GR) and Galactic Center (GC) (Koyama et al. 1996; Kaneda et al. 1997; Ebisawa et al. 2001; Muno et al. 2004). According to this hypothesis, the highly charged ions are low-energy cosmic rays that CX with neutral gas in the plane of the Galaxy. This CX mechanism would naturally explain the remarkable similarity in the spectral shapes of GC and GR diffuse emission from widely separated regions of the Galaxy, since the emission arises from essentially the same population of ions with the intensity level primarily determined by the supply of neutral gas.

A major problem with this idea, however, is that it assumes that cosmic rays remain nearly fully ionized even at low energies (of order 100 keV amu^{-1}). Because of solar modulation, there are no reliable measurements of cosmic ray flux or ionization state below $\sim$1 GeV amu^{-1} (Fulks 1975), but theoretical work on cosmic-ray CX (Watson 1976; Bussard, Ramaty, & Omidvar 1978) predicts that the fraction of fully ionized Fe is negligible below several MeV amu^{-1}. Given existing uncertainties in the cosmic-ray energy budget and flux at low energies, however, a CX explanation for at least some of the GR line emission cannot yet be discounted.

Provided that a 'significant' fraction ($\gtrsim 10^{-4}$) of cosmic rays remains nearly fully ionized at low energies, then even conservative extrapolations of the cosmic ray flux to low energies can account for the observed GR line flux (Raymond & Wargelin, in preparation), and the characteristic collision energy for CX emission is straightforward to predict. Because of the sharp fall-off in CX cross sections at energies above $\sim$25$q^{0.5}$ keV amu^{-1}(Ryufuku & Watanabe 1979), the emission-weighted average collision energy ranges from several tens

to a few hundred keV amu^{-1}, depending on the element and the shape of the low-energy cosmic ray flux distribution. The typical energy for Fe emission will be roughly 200 keV amu^{-1}, corresponding to a line width of $\sim$170 eV. (All line widths in this paper are given in terms of the FWHM.) In comparison, the Doppler broadening for Fe Lyα in a plasma with $kT = 10$ keV is only $\sim$7 eV. Intriguingly, $\sim$170 eV is the line width measured by Koyama et al. (1996) and Tanaka et al. (2000) in an *ASCA* spectrum of the GC, and is also consistent with results from GR spectra (Tanaka 2002). More recently, however, Muno et al. (2004) observed several GC fields with *Chandra* and deduced that line broadening was probably no more than $\sim$ 100 eV and could be consistent with zero.

Unfortunately then, the energy resolution of the *ASCA* and *Chandra* spectra ($\sim$200 eV at 7 keV) is insufficient to permit firm conclusions regarding line broadening, and in both cases energy calibration uncertainties are large enough to prohibit adequately precise line centroid determinations that would distinguish between CX and thermal emission (see §2). The *XRS* microcalorimeter detector on *ASTRO-E2* (Mitsuda et al. 2004), which has 6-eV resolution, should be able to provide definitive measurements although its small field of view will necessitate very long exposures.

We next briefly review the CX mechanism and discuss key diagnostics of CX emission that can be used in the analysis of *ASTRO-E2* spectra. In §3 we describe our experiment, then follow with an explanation of data analysis procedures in §4, discussion of results in §5, and conclusion in §6.

2. CHARGE EXCHANGE THEORY

CX is the radiationless collisional transfer of one or more electrons from a neutral atom or molecule to an ion. If the recipient ion is highly charged it is left in an excited state which then decays via radiative cascades, or else, if the neutral species donates more than one electron, by autoionization.

Since no photons are emitted during the electron transfer, the sum of the internal energies of the ion and atom/molecule are conserved, and the donated electron(s) can be transferred only to specific levels in the ion. The resonant character of the electron transfer is softened somewhat by distortion of the energy levels of ion and atom during the collision, so that a range of atomic states is accessible. For low collision energies (up to $\sim$100 keV amu^{-1}), the n level with the largest capture probability for single-electron transfer is given approximately by Janev & Winter (1985) (rewriting to explicitly include the neutral species

ionization potential) as

$$n_{max} \sim q \left(\frac{I_H}{I_n}\right)^{1/2} \left(1 + \frac{q-1}{\sqrt{2q}}\right)^{-1/2} , \tag{1}$$

where q is the ion charge, I_n is the ionization potential of the neutral species, and I_H is the ionization potential of atomic H (13.6 eV). For Fe^{26+} and Fe^{25+} colliding with H at low energies, n_{max} is therefore expected to be $\sim$12. Molecular nitrogen has an ionization potential of 15.6 eV (14.5 eV for atomic N), so n_{max} for CX with N_2 is nearly the same as with H. (The second ionization potentials of N and N_2 are roughly 30 eV, so the transfer level for the second electron in double-transfer is lower, $n_{max} \sim 8$.) At low collision energies, the n-distribution has a fairly sharp maximum, but gradually broadens to its widest at $\sim 25q^{0.5}$ keV amu^{-1}. At even higher energies, n_{max} slowly decreases and the distribution narrows again (Ryufuku & Watanabe 1979).

The angular momentum (l) distribution varies more strongly with collision energy. The details of this energy dependence are important because they affect how the excited ion can radiatively decay, e.g., directly to ground if $l_{initial} - l_{ground} = \pm 1$, or via cascades for large values of initial l. The l distribution is especially important in the CX of fully stripped ions, which yields excited hydrogenic ions. For example, if the initial excited level is an $11p$ state, it can decay directly to the $1s$ ground state yielding a Lyκ photon. If the ion starts from an s, d, f, g, or other state, however, it cannot decay to ground because of the $\Delta l = \pm 1$ selection rule. Instead, the ion is likely to end up decaying along the "yrast chain" in sequential $\Delta l = \Delta n = -1$ steps with $l = n - 1$ ($\cdots 4f \to 3d \to 2p \to 1s$), ultimately resulting in Lyα emission.

At low collision energies, low-l states are most likely to be populated (Ryufuku & Watanabe 1979) and the combined intensity of high-n lines ($n \geq 3 \to 1$) may exceed that of Lyα (Beiersdorfer et al. 2000). As energy increases, however, the l distribution becomes more statistical in nature (in proportion to $2l + 1$) and fewer of the initial states can decay directly to ground, resulting in a higher fraction of Lyα emission. The hardness ratio of high-n versus Lyα emission can thus be used as a diagnostic of collision energy, as illustrated for O VIII and Ne X by Beiersdorfer et al. (2001).

At the higher energies of relevance for cosmic-ray CX (~ 100 keV amu^{-1}) only a few percent of the X-ray emission is from high-n states. The absence of significant high-n Fe lines in observations of diffuse emission from the Galactic Ridge and Galactic Center therefore does not necessarily indicate the absence of cosmic-ray CX emission (cf. Masai et al. (2002)). Enhanced high-n emission *is* expected, however, when collision energies are low, e.g., for highly charged thermal ions (with collision energies $\ll 1$ keV amu^{-1} even for $kT \sim$ tens of keV). Such a situation may occur in some locations in the Galactic Center, with relatively

narrow CX lines (Doppler widths of order 10 eV—see §1) arising from highly ionized thermal plasma as it interacts with neutral gas on the boundaries of dense molecular clouds.

The hardness ratio of emission from He-like ions is much less sensitive to collision energy because the $n = 2 \rightarrow 1$ line (Kα) always dominates. From simple spin statistics, following electron transfer a He-like ion will have total spin $S = 1$ about 3/4 of the time, and $S = 0$ only 1/4 of the time. Since only $\Delta S = 0$ transitions are allowed, none of the high-n $S = 1$ (triplet) states can decay to the $S = 0$ (singlet) $^1S_0$ ground state, and instead the excited electron cascades to one of the $n = 2$ triplet states from which it ultimately decays via a forbidden or semi-permitted transition.

Within the $n = 2$ level, the triplet $^3P_{2,1}$ and $^3S_1$ states that give rise to the "intercombination" and "forbidden" lines, respectively, receive much more of the cascade-derived population than the singlet $^1P_1$ state that yields the "resonance" line. The triplet lines are therefore much stronger relative to the resonance line in CX spectra than they are in thermal plasmas. (See recent measurements by Beiersdorfer et al. (2003) and theoretical predictions by Kharchenko et al. (2003).) Given adequate energy resolution, this is an excellent indicator of CX emission, regardless of ion-neutral collision energy. As we illustrate in §5.1, however, even if the Kα lines are instrumentally blended one may still be able to use the energy centroid of the blend to distinguish between CX and thermal emission.

3. EXPERIMENTAL METHOD

Our experiment used the Lawrence Livermore National Laboratory (LLNL) EBIT-II electron beam ion trap to collect Fe XXVI and Fe XXV CX spectra using N_2 as the neutral gas. The operation of EBITs has been described extensively elsewhere (Levine et al. 1988) as has the magnetic trapping mode (Beiersdorfer et al. 1996a) used for these measurements. To briefly summarize, Fe ions are injected into the EBIT-II trap region from a metal vapor vacuum arc where they are further ionized and trapped, longitudinally by an electrostatic potential and radially by a 3-T magnetic field, as well as by electrostatic attraction of the narrow electron beam.

The neutral gas is injected directly into the trap where some N_2 molecules CX with the trapped Fe ions before being ionized and dissociated themselves. Although CX cross sections are much larger than those for electron impact excitation (of order 10^{-14} cm^2 versus 10^{-21} cm^2 in this case), the relevant densities and collision velocities are much smaller for CX than for electron-ion collisions, and the net rate of detected CX emission is less than 1% of that from electron excitation. CX spectra are therefore collected in the magnetic trapping mode

with the electron beam turned off once the desired ion charge balance has been attained. The ions are still confined (though less densely) within the trap region, where they collide with neutral nitrogen molecules, undergo CX, and emit photons. Our measurements record the net result of all relevant CX processes, whether from single or multi-electron transfer, radiative decays, or autoionization, as manifested by their spectra.

Two high-purity Ge detectors with energy resolutions of $\sim$ 250 eV and $\sim$ 370 eV (FWHM at 7 keV), were used to collect spectra. The signal-processing lower level discriminators were set at 5 and 4 kev, respectively, to exclude unnecessary events and prevent event pile-up. All the results we present were obtained with the higher-resolution detector, but the second detector with its lower energy threshold was helpful in identifying trap contaminants.

Because the detector resolution was insufficient to directly separate the spectra of Fe XXVI and Fe XXV, data were collected in two measurements using different electron beam energies. The low-energy run (L) used $E_{beam} = 9.2$ keV, and the two high-energy runs (I and J) were at 17.2 keV. For comparison, the ionization potentials of Li-like Fe^{23+}, He-like Fe^{24+}, and H-like Fe^{25+} are 2.046, 8.828, and 9.278 keV, respectively (see Table 1). During run L most of the trapped ions were He-like, with a small fraction of H-like. The observed CX spectrum was therefore a nearly pure He-like spectrum. (The Li-like CX spectrum lies below 2 keV, well below the lower level discriminator setting.) In runs I and J (17.2 keV), the trap contained significant fractions of He-like, H-like, and bare ions, with a roughly 2:1 ratio of Fe^{25+} and Fe^{26+}, resulting in a mixed CX spectrum of He-like Fe XXV and H-like Fe XXVI lines.

In the 31-hour L run, ions were electrostatically trapped and ionized for 3.5 seconds (the beam-on phase), followed by 2.5 seconds of magnetic trapping (the beam-off CX phase). In the I and J runs (18 and 20 hours) the beam-on phase lasted 4.5 seconds. The beam current was $\sim$140 mA in all cases, with a trap electric potential of 300 V for run L and 100 V for I and J. The difference in trap potentials was inadvertent and results in only a small difference in effective ion-neutral collision energies. Based on past measurements of ion energies as a function of trapping parameters (Beiersdorfer et al. 1996b), we estimate the average ion energy in both cases to be very roughly 10 eV amu^{-1}: between 5 and 20 eV amu^{-1} for runs I and J, and approximately double that for run L. Although the Fe XXV CX spectrum was therefore collected under two different conditions, its weak dependence on collision energy, as explained in §2, means that the results from run L can be applied to runs I and J with negligible error, as was confirmed during data analysis.

4. DATA ANALYSIS

4.1. Energy Calibration

Because all the lines of interest are at least partially blended, precise knowledge of the line energies and the detector energy scale is essential for proper spectral fitting. Published line energies were weighted by theoretical cross sections to predict the centroid energies of all relevant emission line blends. Detector energy scales were calibrated by fitting the beam-on spectra (see Figure 1), which have far more counts than the beam-off (CX) data. The CX spectra were then fit using the derived energy calibrations and detailed spectral models.

To simplify analysis and increase the signal-to-noise ratio, and because their spectra were virtually identical, data from runs I and J were combined by scaling the energy/channel relationship of run J by 0.9980 with an offset of +0.077 channels (2.7 eV) and rebinning to match run I. As explained below, the He-like Fe XXV $K\beta$ line was used as an absolute energy reference while radiative recombination (RR) "lines" in the beam-on spectra, which are widely separated with well known energy differences, were used to deduce the scaling factors (eV per detector channel).

4.1.1. Polarization and Effective Line Energies

During the beam-on phase, the unidirectional nature of the electron-ion collisions leads to polarization effects and non-isotropic emission. During the beam-off phase, however, there is no preferred direction for ion-neutral collisions and the resulting CX emission is unpolarized. Each emission line and RR feature is usually a blend of several transitions, so the strength of each transition and its polarization must be known in order to predict the energy centroid of the observed feature.

Table 1 lists theoretical energies of individual levels. Uncertainties are based on comparisons among different sources where possible. Polarization corrections were made according to the prescriptions described by Wong et al. (1995). These corrections have negligible effect on emission line centroids in nearly all cases, but polarization is more important for RR features, as described below.

In H-like Fe XXVI, the simple 2:1 intensity ratio of transitions from $p_{3/2}$ and $p_{1/2}$ levels is slightly modified by polarization adjustments to 2.1:1. For Lyα this shifts the centroid from 6966.0 to 6966.2 eV. Energy shifts for higher-n lines are even smaller.

For He-like emission from $n \geq 3$, selection rules dictate that transitions from $1snp\ ^1P_1$ to

ground dominate, but there are also significant contributions from $1snp\,^3P_1$ levels because of level mixing between states with the same L and J. The $K\beta_2/K\beta_1$ ($^3P_1/^1P_1$) ratio has been measured to be $\sim 1/3$ at 8 and 10 keV (Smith et al. 2000). At higher energies, the excitation cross section for $K\beta_2$ decreases rapidly while that for $K\beta_1$ remains roughly constant for energies up to several times threshold. We therefore assume that $K\beta_2/K\beta_1$ is 0.1 ± 0.1 at 17 keV. For higher n the ratio is smaller than for $n = 3$; the actual values for $n > 3$ are of little importance so we conservatively assume 0.2 ± 0.2 for both 9.2 and 17 keV.

For $K\alpha$, emission from other triplet levels ($^3S_1$ and $^3P_2$) is also important, and the relative intensities of all the lines, which have a relatively large energy spread, can not be predicted accurately. We therefore leave the $K\alpha$ energy free in spectral fits.

Line-energy centroids, appropriate for both the beam-on and beam-off phases, are listed in Table 1. Average energies for RR into $n = 1$ and 2 are also listed and were derived from RR cross sections listed in Table 2. The RR cross sections include polarization effects appropriate for our instrumental geometry (with observations perpendicular to the electron beam axis) and were calculated (Scofield 1989) using matrix elements obtained from a version of the GRASP Code (Parpia et al. 1996) that was modified to calculate the wave functions of the free electrons along with their phase shifts. The extension beyond a central potential model was needed to treat the recombination onto open subshells. Results were extrapolated from $n = 2$ to higher n using the same s- and p-state weightings and assuming that RR into l-levels other than s and p is small. Errors in those assumptions become less important as n increases because the energy spread within a given n-level decreases, and the quoted uncertainties are conservative.

For both emission lines and RR, uncertainties in the weighted energies are driven largely by uncertainties in the energies of individual levels. In the end, errors in the calibration of the energy scale have an insignificant effect on the spectral fitting results.

4.1.2. Beam-On Spectral Fitting

The beam-on spectra were fit using the *Chandra* Interactive Analysis of Observations (CIAO) *Sherpa* fitting package (Freeman, Doe, & Siemiginowska 2001). All lines were fit using Gaussians, in three energy ranges encompassing electron impact excitation (EIE) lines, RR into $n \geq 2$, and RR into $n = 1$ (see Figure 1). Within the EIE group, line energies and widths were linked to those for Fe XXV Kβ, except for the Fe XXV Kα blend and the unresolved K and Lyman series limit blends. Continuum emission (from two-photon radiation, bremsstrahlung, and low-energy tails and other instrumental effects in the Ge
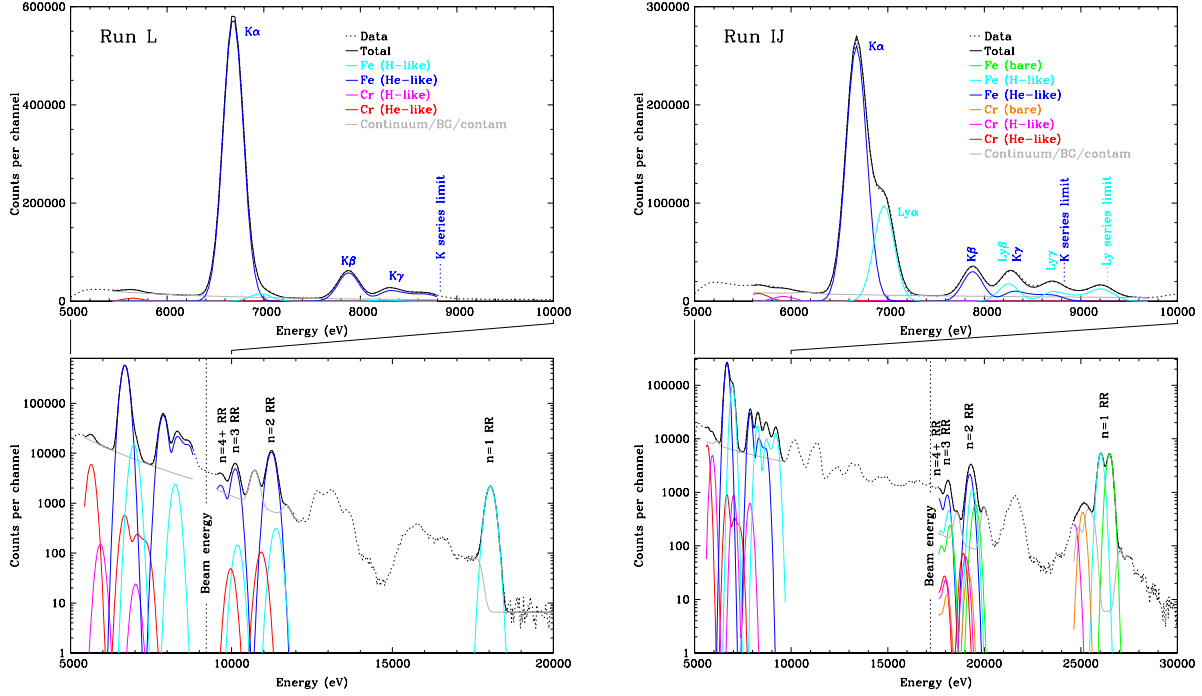
Fig. 1.— Spectra from beam-on phase, with linear (top) and log (bottom) vertical scales. Plots on left are for run L ($E_{beam} = 9.22$ keV), plots on right for run IJ ($E_{beam} = 17.21$ keV). Top panels are close-ups of the electron impact excitation Fe spectra (5–10 keV). These spectra were used to precisely calibrate the energy scales (34.27 eV channel^{-1} for L, 34.62 eV channel^{-1} for IJ) by measuring separations between RR peaks; the Kβ lines were used to fix absolute energies. Cr emission was scaled from corresponding Fe lines, normalized by the fitted ratio of Cr and Fe $n = 2 \rightarrow 1$ lines.

detectors and signal-processing electronics) was fit with power laws. EIE lines from $n = 2 - 7$ and $n \sim n_{limit}$ ($8 - \infty$) were included in the fits, although for $n \geq 5$ the intensities of individual lines could not be reliably constrained.

Contaminants are always present in the trap, usually at an insignificant level and/or with emission at energies that do not interfere with Fe. One exception here was Cr, the presence of which was deduced from its Cr XXIII Kα emission (and Cr XXIV Lyα in run IJ). In run L the He-like Cr Kα intensity is ∼1% of that for Fe Kα; in run IJ the He-like Cr/Fe ratio is 3% with H-like Cr Lyα at 13% of the Fe Lyα intensity. Higher-n Cr EIE and RR lines were included in the fits, with intensities scaled to the corresponding Fe lines. Other contaminant lines (from Ba, Ar, Ti) were included in the RR fits as needed.

In run L, the EIE spectrum was dominated by He-like Fe XXV lines, but there was also a small contribution from Fe XXVI. Fit results for Lyα (with 2.8% the strength of Kα) were

used to scale the H-like $\rightarrow$ He-like $n = 2$ and 3 RR lines relative to their He-like $\rightarrow$ Li-like counterparts.

Fit sensitivities were studied by varying continuum levels, the number of contaminant lines, and links between line energies and widths. In all cases, uncertainties in Fe line positions are dominated by counting statistics, but to be conservative we set the overall line errors equal to double the statistical errors.

For run L, the $n = 1$ RR peak (H-like $\rightarrow$ He-like Fe) and $n = 2$ and 3 RR peaks (dominated by He-like $\rightarrow$ Li-like Fe) were used to determine the energy scale of 34.27 ± 0.03 eV channel^{-1}, and the position of the Fe XXV Kβ line (7878.5 eV) was determined with an accuracy corresponding to ± 1.5 eV. With the absolute energy calibration established, the electron beam energy centroid was measured to be 9217 ± 3 eV.

Run IJ had a more balanced mix of He-like, H-like, and bare Fe ions and thus a complicated blend of lines in the $n = 2$ and 3 RR peaks (with relative intensities of each ion's RR emission fixed at 56:29:15, respectively, based on the $n = 1$ RR fits, Lyα/Kα ratio, and theoretical cross sections for EIE and RR), so the IJ energy scale (34.62 ± 0.06 eV channel^{-1}) was less well calibrated than for the L run. Note that energy scales for the two runs are not expected to be identical because of thermal drifts in the signal-processing electronics. The Fe XXV Kβ line position was slightly less well measured (± 2 eV) than in run L because of the presence of Lyman-series emission, and the electron beam energy was determined to be 17207 ± 16 eV.

4.2. CX Spectral Fitting

For the CX spectra (Figure 2) we first fit the L data and then used those results as a template for the He-like spectrum when fitting the combined He-like and H-like spectra in the IJ data. As was done for the beam-on fits, we modeled the He-like and H-like Cr spectra by fixing their $n \geq 3$ line intensities at a set fraction of their Fe counterparts, based on the fitted Cr Kα/Fe Kα ratio (0.067 for run L and 0.045 for run IJ) and Cr Lyα/Fe Lyα ratio (0.12 for run IJ).

For the L spectrum, all line energies were fixed except for Cr and Fe Kα, and Cr and Fe K$_{limit}$. The Fe Kα and K$_{limit}$ lines also had free widths (with linked Cr line widths); all other line widths were linked to Fe Kβ. The background was fixed at a constant level based on its value at energies above 9.2 keV. Two Ne-like Ba lines at $\sim$5290 and $\sim$6200 eV were also included. Additional Ne-like Ba $n = 3 \rightarrow 2$ lines were seen in the second Ge detector around 4390 and 4550 eV, giving us confidence in these line identifications. Ba is always a
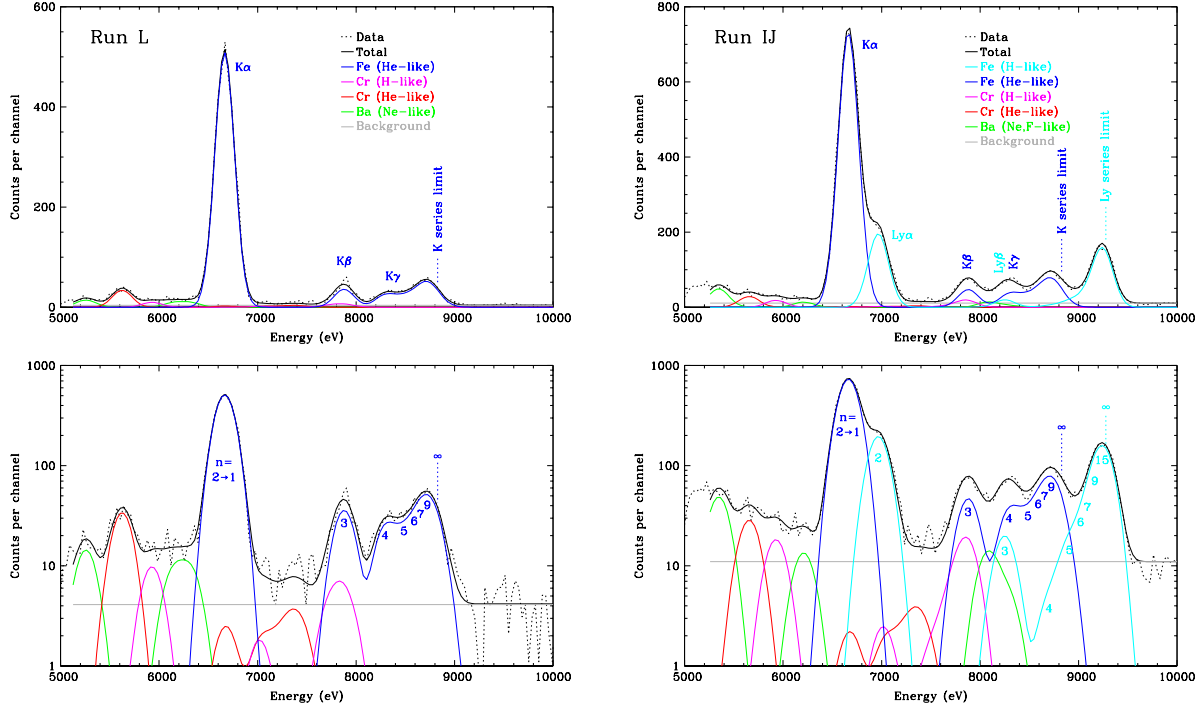
Fig. 2.— Spectra from beam-off (CX) phase. Fit results from run L (He-like spectrum) were scaled relative to Kα when fitting the run IJ spectrum (combined He-like and H-like spectra). Uncertainties for Fe XXVI intensities listed in Table 3 are primarily due to uncertainties in the Fe XXV intensities and the assumed background level.

contaminant in the EBIT-II and comes from the electron gun filament.

For the IJ fits, the He-like Cr and Fe spectra derived from the run L fits were simply normalized to the fitted intensities of Cr Kα and Fe Kα with no other free parameters. All Cr and Fe Lyman line energies and widths were fixed except for the Ly_{limit} lines, with the Cr lines scaled to their Fe counterparts as described above.

As in the L fit, two Ne-like Ba lines were included below Fe Kα and a flat background was assumed. Given the higher beam energy in run IJ (17.21 keV, compared with 8.33 keV for the ionization potential of Ne-like Ba), there is also likely to be some emission from other more highly charged species of Ba. Indeed, there are small but noticeable excesses of emission just below and above the Fe Kγ+Lyβ peak that we attribute to the n_{max} peaks of O-like → F-like and F-like → Ne-like Ba charge exchange.

5.   RESULTS AND DISCUSSION

5.1.   Line Energies

Although the four lines within the Fe XXV Kα complex cannot be resolved, the energy centroid of Kα was measured fairly accurately. In the run-L CX spectrum the Kα blend energy was 6666 ± 5 eV, in contrast to the beam-on centroid of 6685 ± 2.5 eV, a difference of 19 ± 4 eV. (Note that the absolute energy calibration error is the same for both measurements and thus is not included in the difference error.) As explained in §2, a shift is expected because the forbidden and intercombination lines are much stronger (relative to the resonance line) in CX spectra than when excited by electron collisions. A similar but less accurately measured shift was also observed in the IJ fits.

The Fe K_{limit} energy was measured to be 8725 ± 25 eV, corresponding to the energy of the $n = 9 \pm 1$ level. The most likely level of CX electron capture (n_{max}) is probably a little higher than $n = 9$ because the K_{limit} peak is a blend of all lines with $n \geq 8$ and is not resolved from the $n = 6$ or 7 peaks. The approximation given by Eq. 1, $n_{max} \sim 11$ is thus quite good.

The Fe Ly_{limit} peak is much more prominent and narrower than the K_{limit} peak and its energy was measured as 9251 ± 11 eV, which corresponds to $n = 19 \pm 3$. (The ± 11 eV includes a statistical error of ± 7 eV plus 4 eV of energy calibration error.) This is significantly higher than the $n_{max} \sim 11.5$ (corresponding to ~ 9210 eV) expected for CX with N_2 using the approximation from Eq. 1. For CX with atomic H, our theoretical calculations (see §5.3) predict that $n_{max} = 12$ or 13 (~ 9220 eV), versus ~ 12.3 given by Eq. 1.

The K-series emission lies well below the Ly_{limit} peak in energy and there is no evidence for or reason to expect any significant emission from other elements that would shift the Ly_{limit} centroid in our measurement. Double-electron transfer from N_2 is certainly present at some level, but is unlikely to be important. As mentioned in §2, the second electron is most likely to be captured into level $n_{max} \sim 8$, or more than 60 eV lower than the single-electron transfer level (for both Fe^{26+} and Fe^{25+}). Most of the time the resulting doubly excited ion will autoionize and eject the higher-n electron, then radiatively decay and yield a spectrum with enhanced medium-n line emission (relative to the single-electron-transfer spectrum). The high-n peak in the Fe XXVI spectrum shows no non-instrumental broadening, however, and we therefore conclude that double-electron capture is not a signicant contributor to the Fe XXVI Lyman spectrum. If it *were* significant, then the higher-than-expected energy of the Lyman high-n peak would be even more surprising.

5.2. Line Intensities

Fit results are listed in Table 3. Intensity uncertainties are based on counting statistics and sensitivity studies similar to those described in §4.1.2. Some specific variables were the strength of Cr and Ba contaminant lines, but the most important is the level of the background, which is assumed to be flat and arise from particle-induced background in the detector. Another source of uncertainty in our measurements of the Fe XXVI Lyman spectrum is uncertainty in the Fe XXV K spectrum, particularly for the Lyβ line which lies under the stronger Kγ line.

As seen in Table 3, the sum of the $n \geq 3$ Lyman lines exceeds the intensity of Lyα. This relatively large hardness ratio, which we define as the ratio of $n \geq 3 \rightarrow 1$ to $n = 2 \rightarrow 1$ emission, reflects the fact that the collision energy is low and a large fraction of the transferred electrons are captured into low angular momentum states, particularly the $l = 1$ p states (see §2). For comparison, the hardness ratio assuming statistically populated l levels (appropriate at high energies) is ~ 0.02 (Beiersdorfer et al. 2000).

5.3. Comparison with Theory

Theoretical calculations for CX involving molecular targets are much more difficult and unreliable than those for atomic H, so the latter are commonly used for comparison with experimental results. CX with N_2 should produce similar spectra since the major difference when using different neutral gases is some redistribution of intensity among high-n lines because of differences in neutral-gas ionization potentials and hence n_{max} (see, for example, Beiersdorfer et al. (2003)).

Likewise, calculations of bare→H-like CX are much easier to do than for H-like→He-like CX, and we present theoretical results for only the former case. We use detailed classical-trajectory Monte Carlo (CTMC) calculations (Perez, Olson, & Beiersdorfer 2001; Olson 1981) to model Fe^{26+} colliding with atomic H at 1, 10, and 100 eV amu^{-1}. A hydrogenic cascade model is then used to derive emitted line intensities, which are listed in Table 3. The hardness ratio is seen to increase as the collision energy decreases. However, even for collision energies well below those in our experiment, one can see that this model predicts a substantially smaller hardness ratio than we measure. For comparison, measured and theoretical Fe XXVI CX spectra are plotted in Figure 3, along with the measured electron impact excitation spectrum (at 17.2 keV).

Similar disagreements between experimental and theoretical hardness ratios have been noted for other hydrogenic ions, including Ne, Ar, Kr, and Xe (Beiersdorfer et al. 2000), and

our present results confirm the trends established in that work, as illustrated in Figure 4. It is unclear whether these discrepancies are due to multi-electron transfer processes or to l-distributions that are substantially different from the theoretical predictions. Measurements with atomic H and using higher-resolution detectors, which we hope to conduct within the next few years, should resolve these questions. In any event, larger-than-predicted hardness ratios of Fe XXVI and other H-like spectra imply that the signatures of CX in astrophysical sources will be that much easier to detect.

6. CONCLUSIONS

We have presented experimental charge exchange spectra of Fe^{+26} and Fe^{+25} interacting with N_2 at collision energies of ~ 10 eV amu^{-1}. The resulting H-like and He-like spectra show significant enhancement of high-n emission with respect to electron impact excitation spectra. This high-n excess is especially pronounced in the Fe XXVI spectrum and, as has been observed in other measurements at low collision energies, is much stronger than predicted by classical-trajectory Monte Carlo models of CX with atomic H.

Fe CX emission may be detectable in the Galactic Ridge and Galactic Center, arising from cosmic rays or highly ionized thermal gas interacting with neutral clouds in the Galactic plane. Two key diagnostics of this emission are: strong enhancement of forbidden and intercombination line emission in the He-like Kα complex (as exemplified by a 19-eV shift in the blend centroid in our experiment); and enhancement of high-n emission in the H-like Lyman spectrum, particularly if the emission is from thermal ions. Line widths can be used to discriminate between cosmic-ray CX (with widths of order 100 eV FWHM) and thermal CX (less than 10-eV widths). The XRS microcalorimeter on *ASTRO-E2* therefore should be able, given sufficiently deep observations, to clearly identify the spectral signatures of CX in diffuse X-ray emission from the Galactic Center and Galactic Ridge.

REFERENCES

Beiersdorfer, P., et al. 2003, Science, 300, 1558

Beiersdorfer, P., Lisse, C. M., Olson, R. E., Brown, G. V., & Chen, H. 2001, ApJ, 549, L147

Beiersdorfer, P., et al. 2000, Phys. Rev. Lett., 85, 5090

Beiersdorfer, P., Osterheld, A. L., Decaux, V., & Widmann, K. 1996, Phys. Rev. Lett., 77, 5353

Beiersdorfer, P., Schweikhard, L., Crespo López-Urrutia, J., & Widmann, K. 1996, Rev. Sci. Instr., 67, 3818

Bussard, R. W., Ramaty, R., & Omidvar, K. 1978, ApJ, 220, 353

Cravens, T. E. 2002, Science, 296, 1042

Ebisawa, K., Maeda, Y., Kaneda, H., & Yamauchi, S. 2001, Science, 293, 1633

Erickson, G. W. 1977, J. Phys. Chem. Ref. Data, 6, 831

Freeman, P. E., Doe, S., & Siemiginowska A. 2001, SPIE Proceedings, 4477, 76

Fulks, G. J. 1975, J. Geophys. Res., 80, 1701

Janev, R. K., & Winter, H. 1985, Physics Reports, 117, 265

Kaneda, H., Makishima, K., Yamauchi, S., Koyama, K., Matsuzaki, K., & Yamasaki, N. Y. 1997, ApJ, 491, 638

Kharchenko, V., Rigazio, M., Dalgarno, A., & Krasnopolsky, V. A. 2003, ApJ, 585, L73

Koyama, K., Maeda, Y., Sonobe, T., Takeshima, T., Tanaka, Y., & Yamauchi, S. 1996, PASJ, 48, 249

Levine, M. A., Marrs, R. E., Henderson, J. R., Knapp, D. A., & Schneider, M. B. 1988, Phys. Scripta, T22, 157

Masai, K., Dogiel, V. A., Inoue, H., & Schönfelder, V. 2002, ApJ, 581, 1071

Mitsuda, K., Kunieda, H., Inoue, Hajime, & Kelley, R., Proc. SPIE, 5488, 177

Muno, M. P., et al. 2004, ApJ, 613, 326

Olson, R. E. 1981, Phys. Rev. A, 24, 1726

Parpia, F. A., Fischer, C. F., & Grant, I. P. 1996, Computer Phys. Comm., 94, 249

Perez, J. A., Olson, R. E., & Beiersdorfer, P. 2001, J. Phys. B, 34, 3063

Plante, D. R., Johnson, W. R., & Sapirstein, J. 1994, Phys. Rev. A, 49, 3519

Ryufuku, H. & Watanabe, T. 1979, Phys. Rev. A, 20, 1828

Scofield, J. H. 1989, Phys. Rev. A, 40, 3054

Smith, A. J., Beiersdorfer, P., Reed, K. J., Osterheld, A. L., Decaux, V., Widmann, K., & Chen, M. H. 2000, Phys. Rev. A, 62, 012704

Smith, R. K., Edgar, R. J., Plucinsky, P. P., Wargelin, B. J., Freeman, P. E., & Biller, B. A. 2005, ApJ, 623,225

Snowden, S. L., Collier, M. R., & Kuntz, K. D. 2004, ApJ, 610, 1182

Tanaka, Y. 2002, A&A, 382, 1052

Tanaka, Y., Miyaji, T., & Hasinger, G. 1999, Astron. Nachr., 320, 181

Tanaka, Y., Koyama, K., Maeda, Y., & Sonobe, T. 2000, PASJ, 52, L25

Vainshtein, L. A., & Safronova, U. I. 1985, Phys. Scr., 31, 519

Wargelin, B. J., Markevitch, M., Juda, M., Kharchenko, V., Edgar, R., & Dalgarno, A. 2004, ApJ, 607, 596

Watson, W. D. 1976, ApJ, 206, 842

Wong, K. L., Beiersdorfer, P., Reed, K. J., & Vogel, D. A. 1995, Phys. Rev. A, 51, 1214

Table 1.   Fe Ion Energy Levels and Lines

| Ion	Level	Energy (eV)	Reference	Line Energy Centroid (eV)	$E_{RR\ bound}$[a] (eV)
Fe XXVI	$1s$	0	$\cdots$	$\cdots$	0
Fe XXVI	$2p_{1/2}$	6951.9 ± 0.2	1		6956.8 ± 2 @ 9.2 kV
Fe XXVI	$2s$	6952.4 ± 0.2	1	(Lyα) 6966.2 ± 0.3	
Fe XXVI	$2p_{3/2}$	6973.1 ± 0.2	1		6955.3 ± 2 @ 17 kV
Fe XXVI	$3p_{1/2}$	8246.3 ± 0.2	1		
Fe XXVI	$3s$	8246.5 ± 0.2	1	(Lyβ) 8250.5 ± 0.3	8247.5 ± 2
	$3p_{3/2}$	8252.6 ± 0.2	1		
Fe XXVI	$4p_{1/2}$	8698.5 ± 0.2	1		
Fe XXVI	$4p_{3/2}$	8701.1 ± 0.2	1	(Lyγ) 8700.2 ± 0.3	8699.0 ± 1
Fe XXVI	$5p_{1/2}$	8907.4 ± 0.2	1		
Fe XXVI	$5p_{3/2}$	8908.8 ± 0.2	1	(Lyδ) 8908.3 ± 0.3	8908.0 ± 1
Fe XXVI	$6p_{1/2}$	9020.7 ± 0.2	1		
Fe XXVI	$6p_{3/2}$	9021.5 ± 0.2	1	(Lyϵ) 9021.3 ± 0.3	9021.0 ± 1
Fe XXVI	$7p_{1/2}$	9089.0 ± 0.2	1		
Fe XXVI	$7p_{3/2}$	9089.9 ± 0.2	1	(Lyζ) 9089.6 ± 0.3	9089.5 ± 1
Fe XXVI	Ion. Pot.	9277.6 ± 0.2	1	$\cdots$	$\cdots$
Fe XXV	$1s^2$	0	$\cdots$	$\cdots$	0
Fe XXV	$1s2s\ ^3S_1$	6636.7 ± 0.3	2		
Fe XXV	$1s2p\ ^3P_0$	6665.6 ± 0.3	2		
Fe XXV	$1s2p\ ^3P_1$	6667.6 ± 0.3	2		6656.4 ± 3 @ 9.2 kV
Fe XXV	$1s2s\ ^1S_0$	6668.1 ± 0.3	2	(Kα) measured	
Fe XXV	$1s2p\ ^3P_2$	6682.4 ± 0.3	2		6652.8 ± 3 @ 17 kV
Fe XXV	$1s2p\ ^1P_1$	6700.5 ± 0.3	2		
Fe XXV	$1s3s\ ^3S_1$	7863.1 ± 0.3	3		
Fe XXV	$1s3p\ ^3P_1$	7871.1 ± 0.3	3		7868 ± 2 @ 9.2 kV
Fe XXV	$1s3d\ ^3D_2$	7880.3 ± 0.3	3	(Kβ) 7878.5 ± 1.5 @ 9.2 kV	
Fe XXV	$1s3p\ ^1P_1$	7880.9 ± 0.3	3	7880.0 ± 1.5 @ 17 kV	7867 ± 2 @ 17 kV
Fe XXV	$1s3d\ ^1D_2$	7882.3 ± 0.3	3		
Fe XXV	$1s4p\ ^3P_1$	8291.1 ± 0.3	3		
Fe XXV	$1s4p\ ^1P_1$	8295.3 ± 0.3	3	(Kγ) 8294.6 ± 1.0	8290 ± 2
Fe XXV	$1s5p\ ^3P_1$	8485.0 ± 0.3	3		
Fe XXV	$1s5p\ ^1P_1$	8487.1 ± 0.3	3	(Kδ) 8486.8 ± 1.0	8485 ± 2
Fe XXV	$1s6p\ ^3P_1$	8590.0 ± 0.3	4		
Fe XXV	$1s6p\ ^1P_1$	8591.1 ± 0.3	4	(Kϵ) 8590.9 ± 1.0	8590 ± 2
Fe XXV	$1s7p\ ^1P_1$	8653.9 ± 0.3	4	(Kζ) 8653.9 ± 1.0	8653.5 ± 2
Fe XXV	Ion. Pot.	8828.3 ± 0.3	2	$\cdots$	$\cdots$
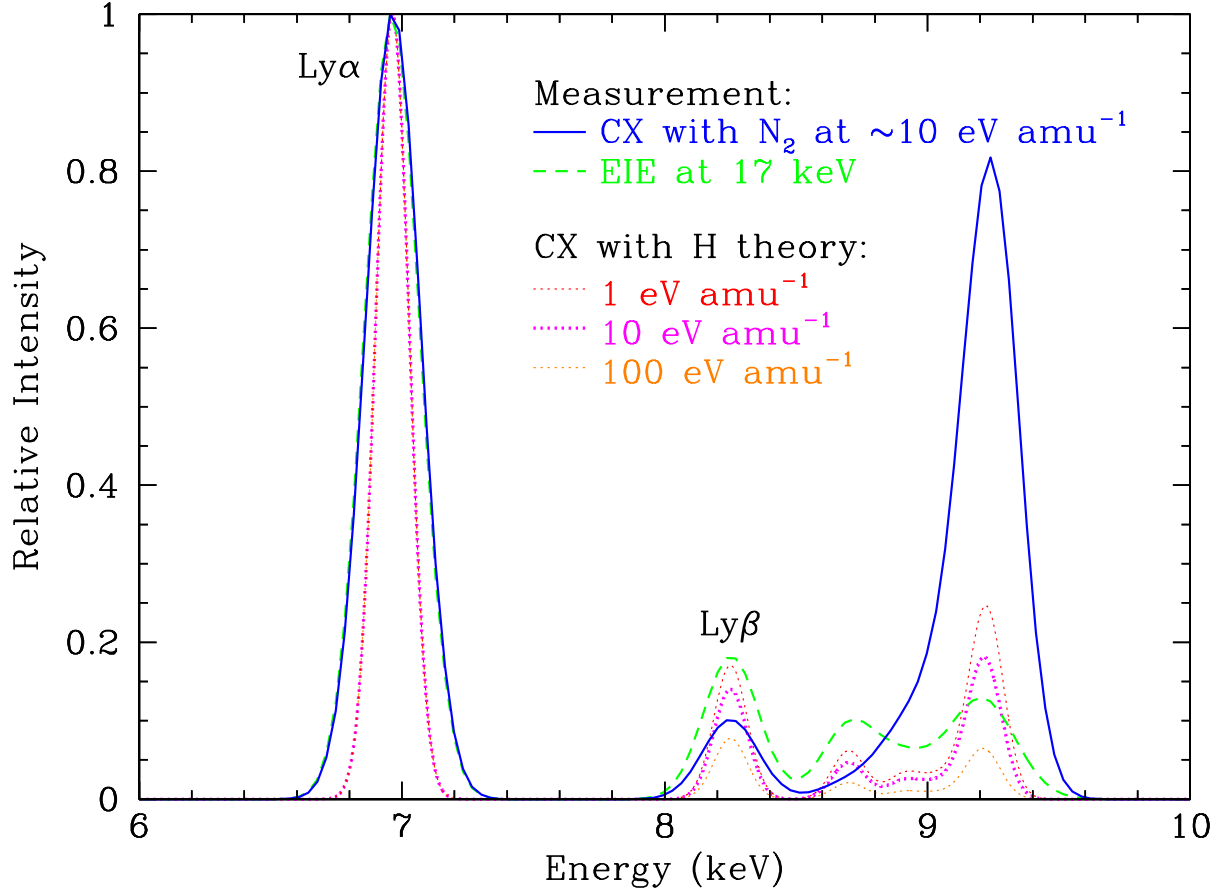
Fig. 3.— Comparison of measured and theoretical Fe XXVI spectra, all normalized to the intensity of Lyα. High-n emission is much stronger in the CX spectra than in the electron impact excitation spectra. The CX high-n peak is also much stronger than predicted by the CTMC model. Theoretical spectra are plotted with better resolution for clarity.
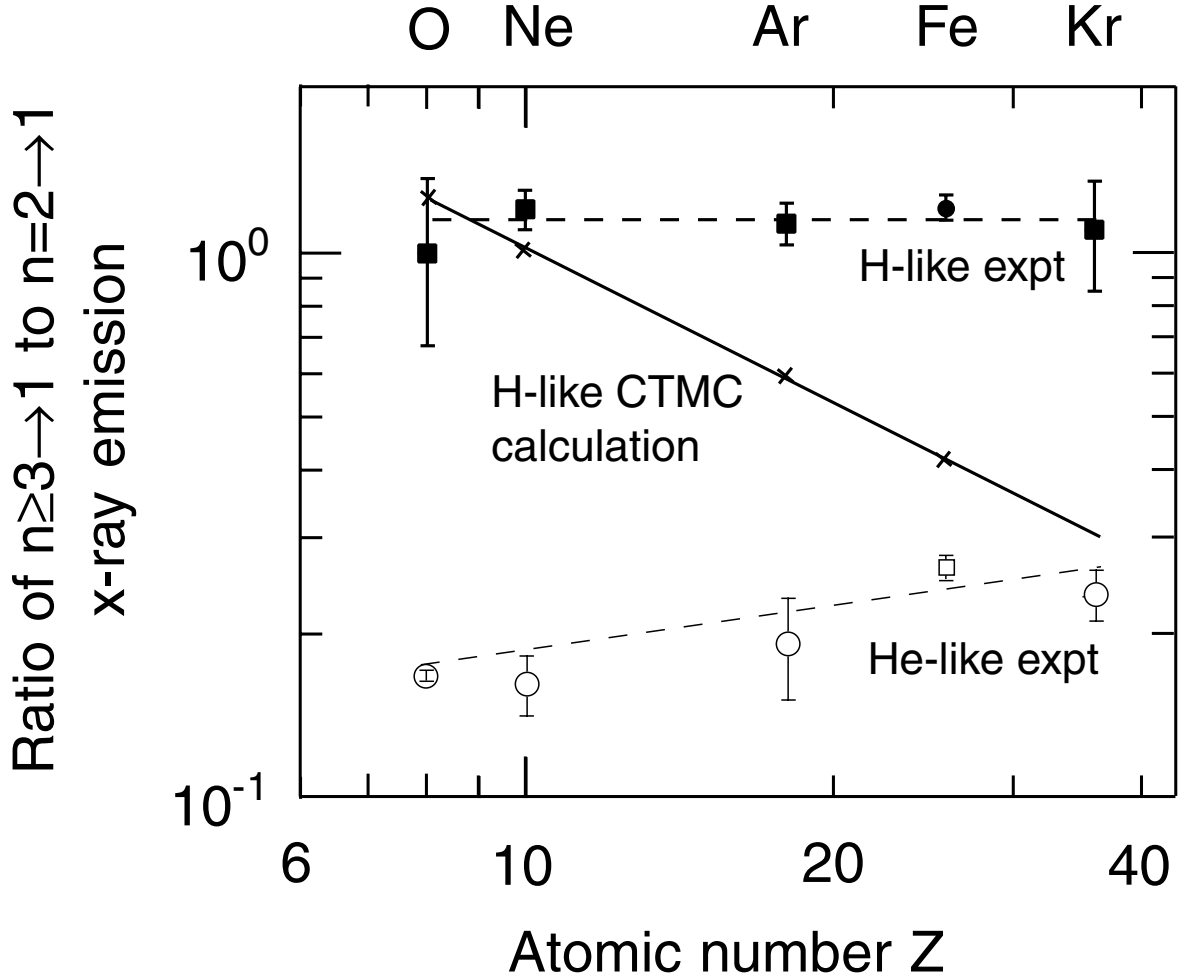
Fig. 4.— Hardness ratios for H-like and He-like CX emission as a function of Z, for collision energies of $\sim$10 eV amu^{-1}. Dashed lines through the H-like measurements (solid points) and He-like measurements (open points) are drawn only to guide the eye. Neutral gases used in the experiments are: CO_2 (for O), Ne (for Ne), Ar (for Ar), N_2 (for Fe), and Kr (for Kr). Results from CTMC calculations ($\times$'s) for CX with atomic H are extrapolated to Kr (solid line). Figure is adapted from that in Beiersdorfer et al. 2000, in which the CTMC curve was inadvertently shifted slightly downward. The H-like O point is from Beiersdorfer et al. 2001, and He-like O is from Beiersdorfer et al. 2003.

Table 1—Continued

Ion	Level	Energy (eV)	Reference	Line Energy Centroid (eV)	$E_{RR\ bound}$[a] (eV)
Fe XXIV	$2s$	0	$\cdots$	below LLD	17.3 ± 3 @ 9.2 kV
Fe XXIV	$2p_{1/2}$	48.7 ± 0.2	3, 5		11.5 ± 3 @ 17 kV
Fe XXIV	$2p_{3/2}$	64.65 ± 0.2	3, 5		
Fe XXIV	$3s$	1149.2 ± 0.3	3, 5	below LLD	1154 ± 2 @ 9.2 kV
Fe XXIV	$3p_{1/2}$	1162.7 ± 0.3	3, 5		1153 ± 2 @ 17 kV
Fe XXIV	$3p_{3/2}$	1167.4 ± 0.3	3, 5		
Fe XXIV	$4s$	1544.9 ± 0.4	3, 5	below LLD	1547 ± 2 @ 9.2 kV
Fe XXIV	$4p_{1/2}$	1550.5 ± 0.4	3, 5		1546 ± 2 @ 17 kV
Fe XXIV	$4p_{3/2}$	1552.5 ± 0.4	3, 5		
Fe XXIV	$5s$	1726.6 ± 0.5	3, 5	below LLD	1727.5 ± 2
Fe XXIV	$5p_{1/2}$	1729.4 ± 0.5	3, 5		
Fe XXIV	$5p_{3/2}$	1730.4 ± 0.5	3, 5		
Fe XXIV	$6s$	1824.7 ± 0.5	3, 5	below LLD	1825 ± 2
Fe XXIV	$6p_{1/2}$	1826.3 ± 0.5	3, 5		
Fe XXIV	$6p_{3/2}$	1826.9 ± 0.5	3, 5		
Fe XXIV	$7s$	1883.7 ± 0.5	5	below LLD	1884 ± 2
Fe XXIV	$7p_{1/2}$	1884.7 ± 0.5	5		
Fe XXIV	$7p_{3/2}$	1885.1 ± 0.5	5		
Fe XXIV	Ion. Pot.	2046.5 ± 1.0	4	$\cdots$	$\cdots$

[a]RR spectral peaks appear at energy $E_{beam} +$ Ion. Pot. $- E_{RR\ bound}$.

References. — (1) Erickson 1977; (2) Plante, Johnson, & Sapirstein 1994; (3) Vainshein & Safronova 1985; (4) This work; (5) D. Liedahl 1998 (private communication) using HULLAC.

Note. — Line energy centroids are the same (within uncertainties) for both EIE (beam-on) and CX (beam-off) spectra, with the exception of the energy for He-like Kα which is left free during spectral fitting. Energy-level weightings for RR into $n = 2$ are based on cross sections listed in Table 2; weightings for higher-n RR were extrapolated, as described in the text.

Table 2.   Radiative Recombination Cross Sections

Ion	Level	$E_{beam} = 5$ keV			$E_{beam} = 8$ keV			$E_{beam} = 11$ keV		
		σ	$\sigma(\theta,\phi)$	P	σ	$\sigma(\theta,\phi)$	P	σ	$\sigma(\theta,\phi)$	P
Fe XXVI	$1s$	226.37	26.422	99.9	120.95	13.989	99.9	76.55	8.775	99.9
Fe XXVI	$2s$	33.57	3.966	100.0	17.52	2.052	99.9	10.89	1.264	99.9
Fe XXVI	$2p_{1/2}$	10.88	1.042	57.6	4.13	0.378	49.6	2.03	0.179	43.8
Fe XXVI	$2p_{3/2}$	20.44	1.969	56.6	7.67	0.706	47.5	3.74	0.332	40.5
Fe XXV	$1s^2$	112.84	13.195	99.9	60.60	7.023	99.9	38.45	4.418	99.9
Fe XXV	$1s2s\,^3S_1$	23.36	2.761	100.0	12.18	1.427	99.9	7.56	0.878	99.9
Fe XXV	$1s2p\,^3P_0$	2.44	0.234	57.3	0.92	0.084	49.1	0.45	0.040	43.2
Fe XXV	$1s2p\,^3P_1$	7.27	0.697	57.2	2.74	0.251	48.9	1.34	0.118	42.9
Fe XXV	$1s2s\,^1S_0$	8.31	0.982	100.0	4.36	0.512	99.9	2.72	0.316	99.9
Fe XXV	$1s2p\,^3P_2$	11.48	1.105	56.3	4.28	0.394	46.9	2.08	0.185	39.9
Fe XXV	$1s2p\,^1P_1$	6.91	0.665	56.4	2.58	0.237	47.1	1.26	0.111	40.2
Fe XXIV	$2s$	29.75	3.517	100.0	15.55	1.823	100.0	9.67	1.124	99.9
Fe XXIV	$2p_{1/2}$	8.69	0.831	56.9	3.26	0.297	48.5	1.59	0.140	42.5
Fe XXIV	$2p_{3/2}$	16.37	1.575	55.9	6.07	0.558	46.4	2.94	0.261	39.3

Ion	Level	$E_{beam} = 14$ keV			$E_{beam} = 17$ keV			$E_{beam} = 20$ keV		
		σ	$\sigma(\theta,\phi)$	P	σ	$\sigma(\theta,\phi)$	P	σ	$\sigma(\theta,\phi)$	P
Fe XXVI	$1s$	53.08	6.031	99.8	39.03	4.395	99.8	29.90	3.338	99.8
Fe XXVI	$2s$	7.44	0.857	99.9	5.41	0.617	99.9	4.11	0.465	99.8
Fe XXVI	$2p_{1/2}$	1.16	0.099	39.5	0.72	0.060	36.0	0.48	0.039	33.3
Fe XXVI	$2p_{3/2}$	2.11	0.182	35.0	1.31	0.110	30.5	0.87	0.072	26.7
Fe XXV	$1s^2$	26.71	3.041	99.9	19.65	2.218	99.8	15.06	1.685	99.8
Fe XXV	$1s2s\,^3S_1$	5.16	0.594	99.9	3.75	0.428	99.9	2.85	0.322	99.8
Fe XXV	$1s2p\,^3P_0$	0.26	0.022	38.8	0.16	0.013	35.4	0.11	0.009	32.7
Fe XXV	$1s2p\,^3P_1$	0.76	0.065	38.4	0.48	0.040	34.9	0.32	0.026	32.1
Fe XXV	$1s2s\,^1S_0$	1.87	0.215	99.9	1.36	0.155	99.9	1.03	0.117	99.8
Fe XXV	$1s2p\,^3P_2$	1.17	0.101	34.4	0.73	0.061	29.8	0.48	0.040	26.0
Fe XXV	$1s2p\,^1P_1$	0.71	0.061	34.8	0.44	0.037	30.4	0.29	0.024	26.8
Fe XXIV	$2s$	6.61	0.762	99.9	4.80	0.549	99.9	3.65	0.413	99.8
Fe XXIV	$2p_{1/2}$	0.90	0.077	38.1	0.56	0.047	34.7	0.38	0.031	32.0
Fe XXIV	$2p_{3/2}$	1.66	0.143	33.7	1.03	0.086	29.2	0.68	0.056	25.4

Note. — Total cross sections σ are in units of 10^{-24} cm^2. Differential cross sections $\sigma(\theta,\phi)$ are for observations perpendicular to the electron beam direction in units of 10^{-24} cm^2 sr^{-1}. Polarizations P are given in

percentages.

Table 3.   Relative Line Intensities

Spectrum	Run or Model	$2 \rightarrow 1$	$3 \rightarrow 1$	$4 \rightarrow 1$	$4^+ \rightarrow 1$	$3^+ \rightarrow 1$
Fe XXV (meas.)	L ($\sim$20 eV amu^{-1})	1	0.074(7)	0.046(5)	0.199(10)	0.273(12)
	IJ ($\sim$10 eV amu^{-1})	1	0.069(7)	$\cdots$	$\cdots$	$\cdots$
Fe XXVI (meas.)	IJ ($\sim$20 eV amu^{-1})	1	0.12(5)	0.04(4)	1.04(7)	1.17(7)
Fe XXVI (theory)	1 eV amu^{-1}	1	0.17	0.06	0.38	0.55
	10 eV amu^{-1}	1	0.14	0.05	0.28	0.42
	100 eV amu^{-1}	1	0.08	0.02	0.10	0.18

Note. — Measurement errors (listed for last digits in parentheses) include both statistical and fitting uncertainties described in the text. Errors for Fe XXVI lines are largely driven by the range of acceptable background levels and by uncertainties in the Fe XXV spectrum. Theoretical CTMC calculations are for CX with atomic H.